Energy resolution of the NEXT-White detector: Part II

NEXT collaboration

J. Renner,[b,1] **G. Díaz López,**[l] **P. Ferrario,**[j,u] **J.A. Hernando Morata,**[l] **G. Martínez-Lema,**[b,l]
F. Monrabal,[p,j] **A. Para,**[g] **J.J. Gómez-Cadenas,**[j,u,2] **C. Adams,**[a] **V. Álvarez,**[b] **L. Arazi,**[c]
C.D.R. Azevedo,[d] **K. Bailey,**[n] **F. Ballester,**[h] **J.M. Benlloch-Rodríguez,**[b] **F.I.G.M. Borges,**[e]
A. Botas,[b] **S. Cárcel,**[b] **J.V. Carrión,**[b] **S. Cebrián,**[f] **C.A.N. Conde,**[e] **J. Díaz,**[b] **M. Diesburg,**[g]
J. Escada,[e] **R. Esteve,**[h] **R. Felkai,**[b] **A.F.M. Fernandes,**[i] **L.M.P. Fernandes,**[i] **A.L. Ferreira,**[d]
E.D.C. Freitas,[i] **J. Generowicz,**[j] **A. Goldschmidt,**[k] **D. González-Díaz,**[l] **R. Guenette,**[a]
R.M. Gutiérrez,[m] **K. Hafidi,**[n] **J. Hauptman,**[o] **C.A.O. Henriques,**[i] **A.I. Hernandez,**[m] **V. Herrero,**[h]
S. Johnston,[n] **B.J.P. Jones,**[p] **M.Kekic,**[b] **L. Labarga,**[q] **A. Laing,**[b] **P. Lebrun,**[g]
N. López-March,[b] **M. Losada,**[m] **R.D.P. Mano,**[i] **J. Martín-Albo,**[a] **A. Martínez,**[b] **A.D. McDonald,**[p]
C.M.B. Monteiro,[i] **F.J. Mora,**[h] **J. Muñoz Vidal,**[b] **M. Musti,**[b] **M. Nebot-Guinot,**[b] **P. Novella,**[b]
D.R. Nygren,[p,2] **B. Palmeiro,**[b] **J. Pérez,**[b,3] **F. Psihas,**[p] **M. Querol,**[b] **J. Repond,**[n] **S. Riordan,**[n]
L. Ripoll,[r] **J. Rodríguez,**[b] **L. Rogers,**[p] **C. Romo-Luque,**[b] **F.P. Santos,**[e] **J.M.F. dos Santos,**[i]
A. Simón,[b] **C. Sofka,**[s,4] **M. Sorel,**[b] **T. Stiegler,**[s] **J.F. Toledo,**[h] **J. Torrent,**[j] **J.F.C.A. Veloso,**[d]
R. Webb,[s] **J.T. White,**[s,3] **N. Yahlali**[b]

[a]*Department of Physics, Harvard University*
  Cambridge, MA 02138, USA

[b]*Instituto de Física Corpuscular (IFIC), CSIC & Universitat de València*
  Calle Catedrático José Beltrán, 2, 46980 Paterna, Valencia, Spain

[c]*Nuclear Engineering Unit, Faculty of Engineering Sciences, Ben-Gurion University of the Negev*
  P.O.B. 653 Beer-Sheva 8410501, Israel

[d]*Institute of Nanostructures, Nanomodelling and Nanofabrication (i3N), Universidade de Aveiro*
  Campus de Santiago, 3810-193 Aveiro, Portugal

[e]*LIP, Department of Physics, University of Coimbra*
  P-3004 516 Coimbra, Portugal

[f]*Laboratorio de Física Nuclear y Astropartículas, Universidad de Zaragoza*
  Calle Pedro Cerbuna, 12, 50009 Zaragoza, Spain

[g]*Fermi National Accelerator Laboratory*
  Batavia, Illinois 60510, USA

[1]corresponding author.
[2]NEXT Co-spokesperson.
[3]Now at Laboratorio Subterráneo de Canfranc, Spain.
[4]Now at University of Texas at Austin, USA.
[5]Deceased.

^{h}*Instituto de Instrumentación para Imagen Molecular (I3M), Centro Mixto CSIC - Universitat Politècnica de València*
Camino de Vera s/n, 46022 Valencia, Spain

^{i}*LIBPhys, Physics Department, University of Coimbra*
Rua Larga, 3004-516 Coimbra, Portugal

^{j}*Donostia International Physics Center (DIPC)*
Paseo Manuel Lardizabal 4, 20018 Donostia-San Sebastian, Spain

^{k}*Lawrence Berkeley National Laboratory (LBNL)*
1 Cyclotron Road, Berkeley, California 94720, USA

^{l}*Instituto Gallego de Física de Altas Energías, Univ. de Santiago de Compostela*
Campus sur, Rúa Xosé María Suárez Núñez, s/n, 15782 Santiago de Compostela, Spain

^{m}*Centro de Investigación en Ciencias Básicas y Aplicadas, Universidad Antonio Nariño*
Sede Circunvalar, Carretera 3 Este No. 47 A-15, Bogotá, Colombia

^{n}*Argonne National Laboratory,*
Argonne IL 60439, USA

^{o}*Department of Physics and Astronomy, Iowa State University*
12 Physics Hall, Ames, Iowa 50011-3160, USA

^{p}*Department of Physics, University of Texas at Arlington*
Arlington, Texas 76019, USA

^{q}*Departamento de Física Teórica, Universidad Autónoma de Madrid*
Campus de Cantoblanco, 28049 Madrid, Spain

^{r}*Escola Politècnica Superior, Universitat de Girona*
Av. Montilivi, s/n, 17071 Girona, Spain

^{s}*Department of Physics and Astronomy, Texas A&M University*
College Station, Texas 77843-4242, USA

^{u}*IKERBASQUE, Basque Foundation for Science*
48013 Bilbao, Spain.

E-mail: josren@uv.es

ABSTRACT: Excellent energy resolution is one of the primary advantages of electroluminescent high pressure xenon TPCs in searches for rare physics events requiring precise energy measurements, such as neutrinoless double-beta decay. The NEXT-White (NEW) detector, developed by the NEXT (Neutrino Experiment with a Xenon TPC) collaboration, has already demonstrated good energy resolution at high energies (up to 1.6 MeV), which was shown to extrapolate to approximately 1% FWHM at the Q-value of neutrinoless double-beta in xenon. Further study with calibration sources, reported here, shows that this resolution is obtainable at 2.6 MeV and therefore demonstrates the potential applicability of the present technology in a neutrinoless double-beta search with ~1% FWHM resolution.

Contents

1 Introduction

Searches for neutrinoless double beta decay ($\beta\beta0\nu$), the observation of which would imply total lepton number violation and show that neutrinos are Majorana particles [1–4], require excellent energy resolution to eliminate background events that occur at energies similar to the Q-value of the decay ($Q_{\beta\beta}$). The NEXT (Neutrino Experiment with a Xenon TPC) collaboration [5–8] intends to search for $\beta\beta0\nu$ using $\sim$ 100 kg of xenon enriched to 90% in the candidate isotope ^{136}Xe ($Q_{\beta\beta}$= 2457.8 keV). In recent years, NEXT has developed and operated several gaseous xenon TPCs, including $\sim$ kg-scale detectors at Lawrence Berkeley National Lab (LBNL) and Instituto de Física Corpuscular (IFIC) [9, 10] and more recently the $\sim$ 5 kg-scale NEXT-White (NEW)[1] at the Canfranc Underground Laboratory (LSC) in the Spanish Pyrenees [11].

The NEW detector has previously shown [12] using gammas produced by ^{137}Cs and ^{232}Th sources that an energy resolution extrapolating to approximately 1% FWHM at the xenon $Q_{\beta\beta}$ was obtainable. Because of the relatively lower pressure (7.2 bar) at which this data was obtained, electron tracks of events with energy near $Q_{\beta\beta}$ were not easily contained in the detector, and the resolution was measured for energies up to 1.6 MeV. More data has since been taken at a higher pressure (10.3 bar), and the energy resolution was measured directly to be approximately 1% at 2.6 MeV, after correcting for effects due to geometric variations, electron lifetime, and another detector phenomenon, the origins of which are still presently being studied. These updated results are reported in the present study. The experimental setup, similar to that of the previous study [12], is reviewed in section 2, and the analysis and obtained energy resolution is presented in section 3.
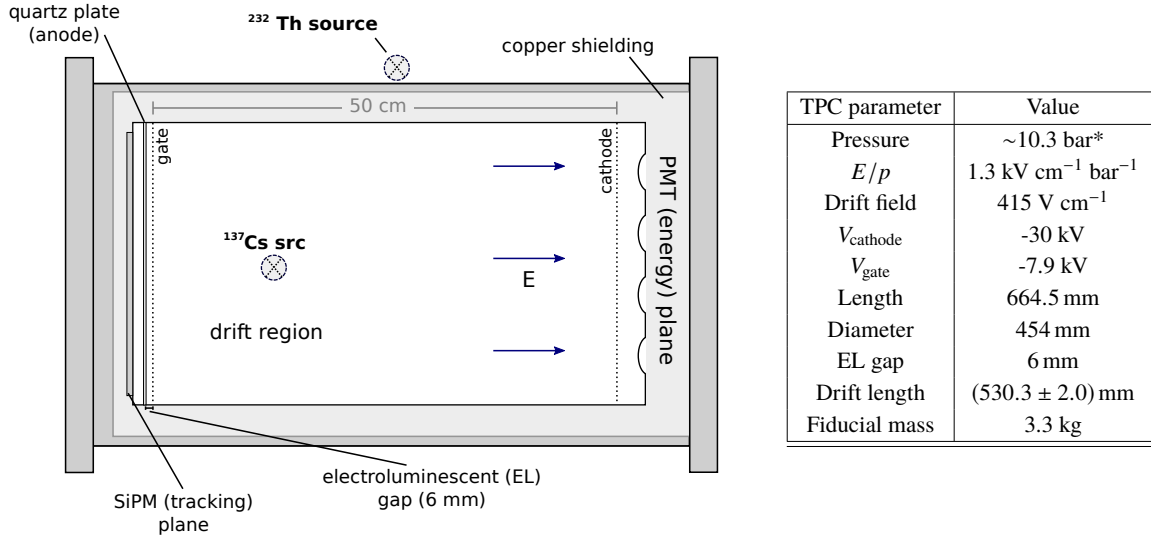
Figure 1: Experimental summary. (Left) Schematic of the main detector components and locations of the calibration sources (not drawn to scale). The ^{137}Cs and ^{232}Th sources were placed in the lateral and top entrance ports of the pressure vessel respectively. This figure was slightly modified from its original version in [12], for which the setup was nearly identical. (Right) NEXT-White operational parameters used in the present study. *The actual measured pressures for each run varied between 10.27-10.32 bar, with one run (6342) taken at 10.48 bar.

2 Experimental setup

2.1 The NEXT-White electroluminescent TPC

The experimental setup is similar to that of the preceding study [12] and is summarized here. The detector NEXT-White is an electroluminescent (EL) time projection chamber (TPC) filled with xenon gas and equipped with photosensors to detect the UV light emitted in interactions occurring within the active volume. Charged particles, for example energetic electrons produced in double-beta decay or photoionization of xenon atoms by gamma rays, deposit energy within the drift region, producing a track of ionized and excited xenon atoms. The UV light emitted in the relaxation of the excited xenon atoms, called primary scintillation or S1, is detected immediately and the ionized electrons are drifted toward a readout plane consisting of a narrow region of high electric field, the EL gap. In passing through the EL gap, the electrons are accelerated to energies high enough to futher excite, but not ionize, the atoms of the xenon gas, leading to the production of an amount of secondary scintillation photons (S2) proportional to the number of electrons traversing the gap. This amplification process, electroluminescence, allows for gains on the order of 1000 photons per electron with significantly lower fluctuations than avalanche gain. In addition, the time elapsed between the observation of S1 and the arrival of S2 can be used to determine the axial (z) coordinate at which the interaction took place.

In NEXT-White (see Figure 1 and also [11]), the primary (S1) and secondary (S2) scintillation are detected by an array of 12 Hamamatsu R11410-10 photomultiplier tubes (PMTs), called the

---

[1]Named after our late mentor and friend Prof. James White.

Table 1: Summary of data analyzed in this study.

Run #	Duration	Avg. Rate	Triggers (low E)	Triggers (high E)	Avg. Lifetime (μs)
6342	23.1 h	41 Hz	3 208 188	281 052	2621
6346	25.0 h	42 Hz	3 485 555	313 761	3977
6347	23.6 h	41 Hz	3 250 612	304 948	4190
6348	23.5 h	41 Hz	3 210 597	307 397	4297
6349	23.8 h	41 Hz	3 248 563	311 204	4261
6351	23.9 h	41 Hz	3 260 929	311 951	4008
6352	24.6 h	41 Hz	3 345 650	321 545	3908
6365	24.4 h	41 Hz	3 300 055	318 662	3344
6482	26.7 h	41 Hz	3 257 113	739 668	3527
6483	24.7 h	41 Hz	3 006 991	684 718	3579
6484	24.4 h	41 Hz	2 959 826	681 687	3586
6485	20.3 h	41 Hz	2 453 528	566 984	3597

"energy plane" placed 130 mm from a transparent wire mesh cathode held at negative high voltage. An electric field is established in the drift region defined by the cathode and another transparent mesh (the "gate") located about 53 cm away. The EL region is defined by the mesh and a grounded quartz plate coated with indium tin oxide (ITO), placed 6 mm behind it. A dense grid (10 mm pitch) of 1792 SensL series-C silicon photomultipliers (SiPMs) is located behind the EL gap and measures the S2 scintillation, providing precise information on where the EL light was produced in (x, y). The active volume is shielded by an 60 mm thick ultra-pure inner copper shell, and the sensor planes are mounted on pure copper plates of thickness 120 mm. The sensor planes and active volume are enclosed in a pressure vessel constructed from the titanium-stabilized stainless steel alloy 316Ti. The vessel sits on top of a seismic table, and a lead shield that can be mechanically opened and closed surrounds the vessel. The vessel is connected to a gas system though which the xenon gas is continuously purified via the use of a hot getter. The entire experimental area, including gas system, electronics, pressure vessel, and seismic table, are stationed on an elevated tramex platform in the Laboratorio Subterráneo de Canfranc (LSC) in the Spanish Pyrenees.

2.2 Run configuration

As the goal of the present analysis was a detailed study of energy resolution, calibration sources were employed to yield energy peaks over a range of energies from several tens of keV up to and including $Q_{\beta\beta}$. ^{83m}Kr was injected into the xenon gas, providing a uniform distribution of 41.5 keV point-like energy depositions used to map out the geometric variations in the sensor responses and electron lifetime of the detector [13]. ^{137}Cs and ^{232}Th calibration sources were also placed in source entrance ports built into the vessel as shown in Figure 1. The ^{137}Cs source provided 661.6 keV gamma rays, and ^{232}Th decays to ^{208}Tl which provides gammas of energy 2614.5 keV. In this study we focus on the energy peaks produced by interactions of these ^{137}Cs and ^{208}Tl gammas, and also the double-escape peak resulting from e^+e^- pair production interactions of the ^{208}Tl gamma in which the two 511 keV gammas (emitted when the e^+ stops and annihilates on an electron) escape.

For the present analysis, the acquisition trigger was split into a lower-energy trigger targeting the ^{83m}Kr events and a high-energy trigger aimed at capturing events with energy above ~ 150 keV. A summary of the datasets analyzed is given in Table 1. For each run, the low-energy triggers were used to compute the lifetime and geometric correction maps used to correct the events acquired with the high-energy trigger. The average electron lifetime determined over the course of the analyzed runs is also shown in Figure 2.
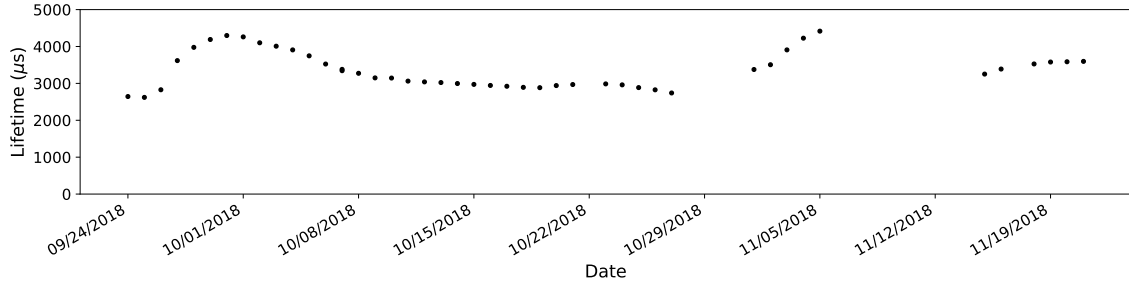
Figure 2: The average electron lifetime over the course of the analyzed runs determined using ^{83m}Kr events.

The energy spectrum of high-energy triggers in the full active volume is shown in Figure 3 after applying all corrections described in section 3 below. Unlike in the previous study [12], the ^{208}Tl photopeak at 2615 keV (near $Q_{\beta\beta}$) is clearly resolved. The energy conversion from detected photoelectrons to keV was determined (after application of all corrections) using a quadratic fit to the means of the three peaks of interest (662 keV, 1592 keV, 2615 keV) and the 29.7 keV K-α xenon x-ray peak. The x-rays had energies too low to be triggered on as individual events, but their energies were visible upon examining the spectrum of isolated energy depositions within all events, which included small depositions due to xenon x-rays that managed to travel away from the main track before interacting.
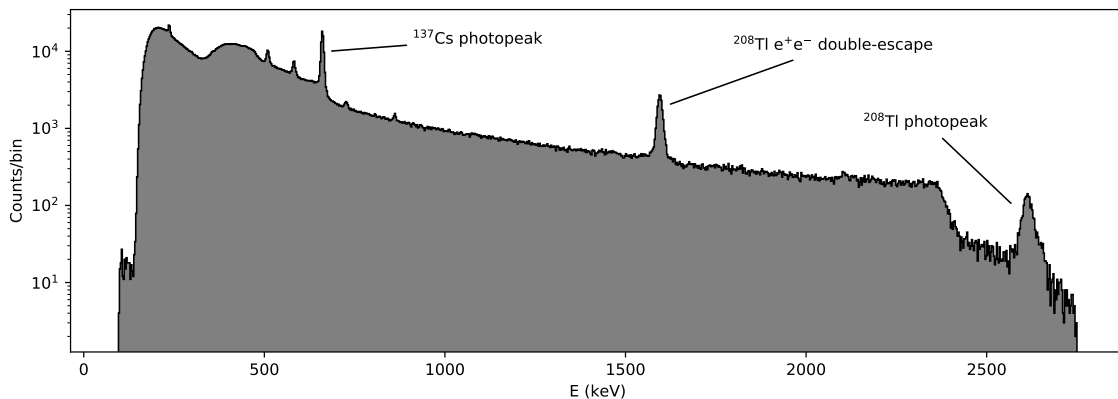

Figure 3: The full energy spectrum for events with energies greater than ~ 150 keV. Corrections for electron lifetime and geometrical effects were applied to all events, as well as a correction for the described axial length effect (see section 3) corresponding to $(m/b) = 2.84 \times 10^{-4}$.

3 Energy resolution

3.1 Data analysis

The signals from the SiPMs and PMTs were digitized in samples of width 1 μs and 25 ns respectively, and the resulting waveforms are analyzed with a Python-based analysis chain. The analysis found the individual pulses in the energy plane waveform (summed over all PMTs, see Figure 4) and classifies them as S1 (short bursts of primary scintillation) or S2 (longer pulses produced by EL light). Events with a single identified S1 were selected, and the S2 peaks were divided into "slices" of width 2 μs.
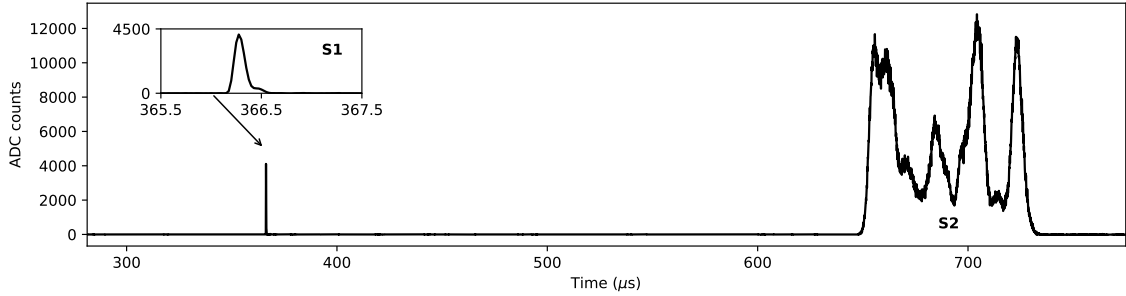
Figure 4: The acquired waveform, summed over all PMTs, for an event in the ^{208}Tl photopeak. Note that this particular event was identified to contain a single continuous track, as evident partially in the existence of a single long S2 pulse.

The pattern of light detected by the SiPMs of the tracking plane during the 2 μs interval of the slice was used to reconstruct the (x, y) location of the EL production, as done in [13], except multiple reconstructed positions sharing the energy E of a single slice were possible, to allow for reconstruction of long tracks that may double-back on themselves. The time elapsed since the S1 pulse was used to determine the z coordinate of each slice, and the energies E of the reconstructed depositions (x, y, z, E) were then multiplied by two correction factors: one accounting for the geometrical (x, y) dependence of the light collection over the EL plane, and another accounting for losses due to the finite electron lifetime caused by attachment to impurities. This second factor depended on the drift length (z-coordinate) and the location in the EL plane (x, y), as the electron lifetime also varied in (x, y). Once fully reconstructed, fiducial cuts were made on each event as detailed in Figure 5.

A final correction was made for an effect that is not fully understood at the time of this writing but is likely to be a physical phenomenon affecting the light production and/or detection processes within the detector. Due to this effect, the measured energy of an event decreases with increasing axial (z) extent of the track. The z-extent Δz is defined as the difference between the maximum and minimum z-coordinates of all reconstructed slices in the event. The effect is shown in Figure 6 along with the resolution obtained for each of the three peaks (662 keV, 1592 keV, and 2615 keV) after correcting for the effect using in each case a normalized slope determined by a linear fit to the distribution,

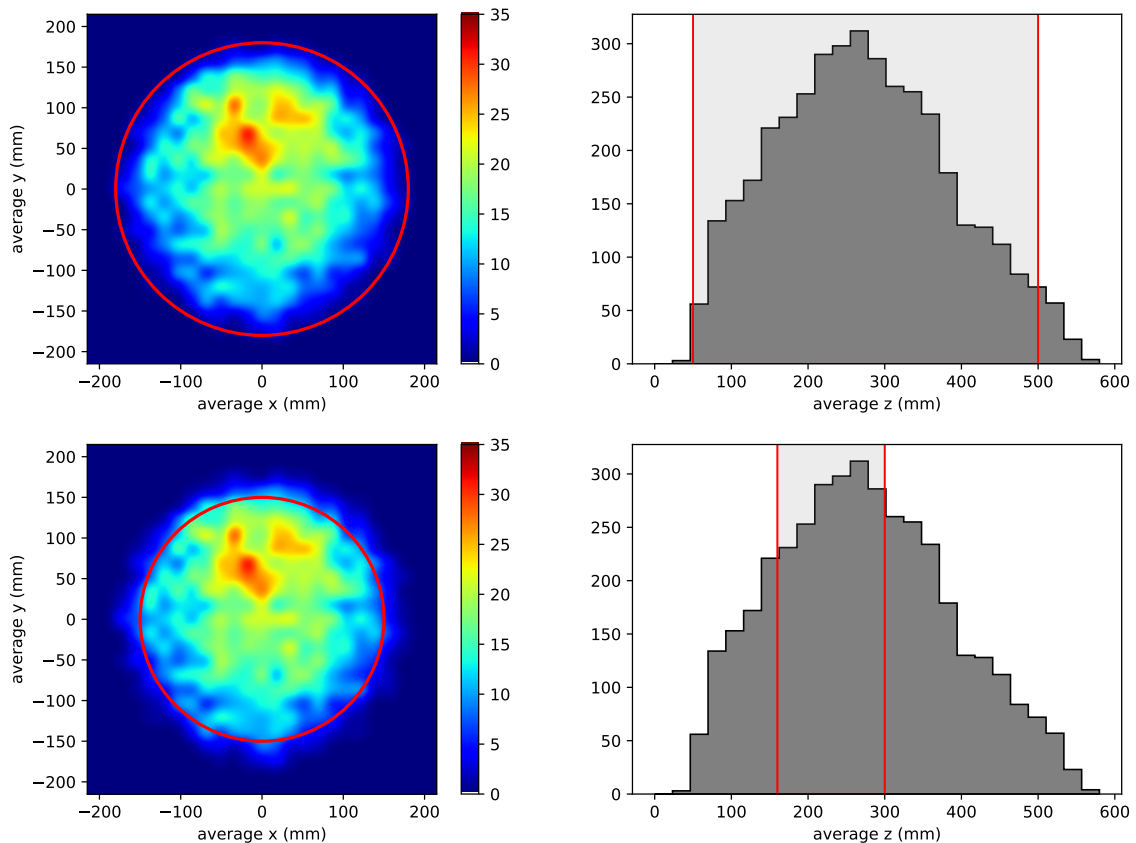$$E_{\text{corrected}} = \frac{E}{1 - (m/b)\Delta z},$$

(3.1)

Figure 5: Distribution in average location, *x*-*y* (left) and *z* (right), of observed events in the 2615 keV ^{208}Tl photopeak. The solid red lines show the "wide" (above) and "tight" (below) fiducial cuts employed in this study. The wide cuts encompass nearly the entirety of the active volume and are used throughout most of the study, while the tight cuts match those used in a previous study [12] and are used only in Figure 7.

where *m* and *b* are the slope and intercept of the linear fit for Δz in mm. As it is not known how the effect differs when an event has multiple sites of energy deposition (due to for example Compton scattering), the events shown in Figure 6 used in determining the correction factors were all required to have been reconstructed as single continuous tracks. Note that the linear fits were performed on the events between the dashed lines, placed by eye (reasonable variations on the positioning of these lines gave an error of approx. 0.2×10^{-4} for each computed slope). Each peak was fit to the sum of a Gaussian and another function to account for the surrounding distribution of background events, and the resolution was computed using the width of the Gaussian. The obtained resolutions are: $1.25 \pm 0.02\%$ FWHM at 662 keV (fit to a Gaussian + 2nd-order polynomial); $1.03 \pm 0.02\%$ FWHM at 1592 keV (fit to a Gaussian + exponential); and $1.06 \pm 0.1\%$ FWHM at 2615 keV (fit to a Gaussian + 2nd-order polynomial). The errors are estimated in each case based on the systematics of variations in the range of events included in the fit and the correction for the axial length effect. Also in each case the corresponding resolution at $Q_{\beta\beta}$, denoted $R_{\beta\beta}$, is computed assuming a $\sim 1/\sqrt{E}$ energy scaling. Because in this case the peaks were corrected using different values of (m/b), their

means have been intentionally scaled to their true values - these energies are therefore not the result of a single calibration such as the one applied in Figure 3.
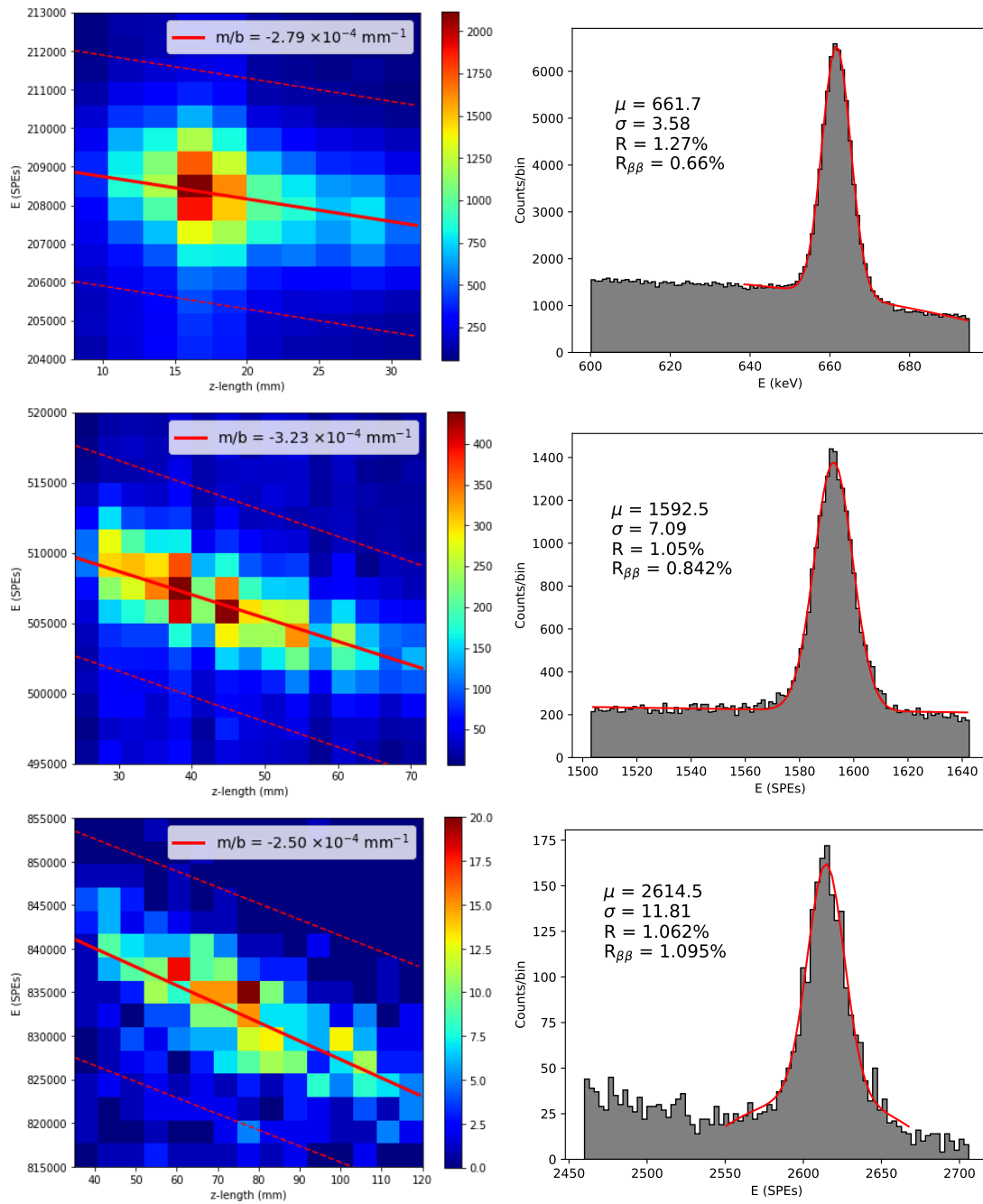

Figure 6: Fits to the dependence of energy on track length in the axial dimension (left), and the resulting energy spectra of three energy peaks after application of all corrections, including a linear correction to the energy (equation 3.1) corresponding to the slope *m* and intercept *b* obtained in the fit (right).

Though this exercise demonstrates that excellent energy resolution is obtainable throughout the

entire fiducial volume once correction for the axial length effect is made, the effect itself complicates the analysis and appears to vary across the different energy peaks. It must be understood and is discussed further in the following section. Note that the resolution can still be improved slightly by introducing the tighter fiducial cuts, as shown in Figure 7. Here cuts were made on the minimum and maximum values of the Z-coordinates of all reconstructed slices (Z_{min} and Z_{max}) and the maximum radial coordinate R_{max} of all reconstructed slices in an event. These cuts were the same as those employed in [12]: 160 mm < Z_{min}, Z_{max} < 300 mm, R_{max} < 150 mm. With these cuts in addition to the correction for the axial length effect the resolution improves to $1.23 \pm 0.02\%$ FWHM at 662 keV; $0.96 \pm 0.02\%$ FWHM at 1592 keV ; and $0.8 \pm 0.1\%$ FWHM at 2615 keV.
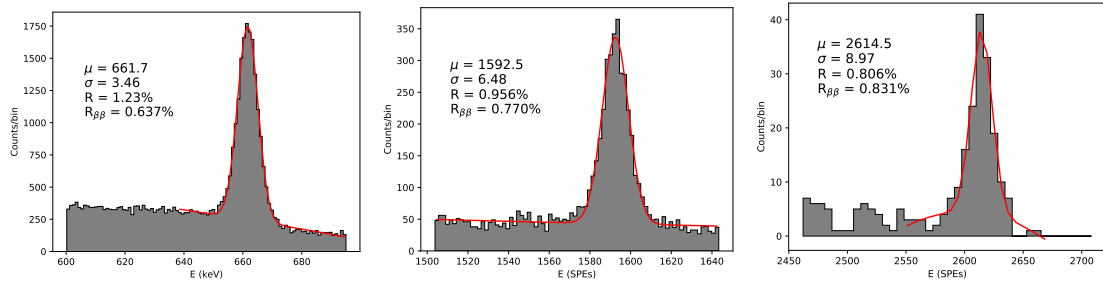

Figure 7: Fits similar to those of Figure 6 but with additional "tight" fiducial cuts of 160 mm < Z_{min}, Z_{max} < 300 mm, R_{max} < 150 mm.

3.2 The axial length effect

It is not presently known what gives rise to the apparent decrease in detected energy with increasing axial length, but several explanations have already been considered and found to be unlikely:

- **PMT saturation / baseline shift:** due to the AC-coupled PMT readout scheme used in NEXT-White [11], all PMT waveforms must be passed through a deconvolution algorithm to remove distortions introduced by high-pass filtering before beginning physics analysis. It was found that if the response of a PMT saturates, the deconvolution may lead to a shifted baseline which could lead to an error in the signal integration (energy) dependent on the length of integration in time (z). However, the effect was found to persist even after lowering PMT gains, ensuring no saturation, and it was confirmed that any shift in baseline present after the deconvolution was not significant enough to account for the effect.

- **Recombination:** as the electrons are drifted in the z-dimension towards the EL plane, it was proposed that tracks extended in this dimension present a greater opportunity for drifting electrons to encounter neighboring ions and recombine. Since these electrons would not arrive at the EL plane and produce light, this would lead to a lower energy measurement. However, basic simulations concluded that the recombination capture radius would need to be on the order of several tens of μm to explain the effect, an unphysically large sphere of influence for a single ion. In addition, electron-ion recombination would lead to scintillation light that should be observable during a time interval beginning after primary scintillation and ending after an amount of time required to drift the electrons over the entire track length in z. For

^{208}Tl photopeak events (see Figure 6, bottom), this would be about 120 μs, and integrating over this interval after the arrival of S1 for many such events, no evidence of the expected light was observed.

- **Variations in electron lifetime:** as the measured electron lifetime in NEXT-White is known to vary with location in the detector, there has been concern that small errors in the computation of the lifetime were giving rise to the observed effect when applied over long tracks. However, even after correcting Cs-photopeak events using a single average position (assuming pointlike tracks), the effect could still be observed by making a tight cut on average radius (effectively eliminating the error due to response variations in the xy-plane by considering only events that did not require significant xy correction).

- **Light emitted from the SiPMs:** the effect is also seen in the integrated charge of the SiPMs, and in fact is more dramatic (the normalized slopes m/b analogous to those shown in Figure 6 are greater in magnitude). Therefore it was proposed that the SiPMs may be emitting additional light in a nonlinear manner during the production of EL. However, even after turning off the SiPM plane and using only information from the PMT plane for a less-precise xy reconstruction, the effect was still observed.

Several explanations for the effect have not yet been investigated in detail:

- **"Charge-up" effect at the EL plane:** an electron crossing the EL gap may, at least locally, alter the electric field seen by the next electron crossing the gap for some amount of time. If this were to make the average gain somewhat dependent on track orientation - whether the electrons cross the gap more in "series" (more extended in z) or in "parallel" (more extended in xy) - this could give rise to the observed effect.

- **Attachment to ionized impurities in the EL gap:** The wavelength shifter tetraphenyl butadiene (TPB) is deposited on several components in NEW, including the quartz plate just behind the EL region, to shift the VUV scintillation produced by xenon to visible light that can be detected by the photosensors (the SiPMs are not VUV sensitive, and the PMTs are placed inside enclosures behind sapphire windows, which do not transmit VUV light, to shield them from the high pressure environment inside the detector). If the photons produced in electroluminescence are capable of photoionizing the TPB, the resulting ions would be drifted across the EL region, possibly capturing some of the electrons that arrived at later times before completely traversing the EL gap and thereby reducing the observed energy of the event.

The observed effect could also be a result of a nonlinearity in the light production process caused by some other internal component. Further investigation in future runs with NEXT-White, possibly involving alterations of the internal hardware and/or running systematically at different EL gains, will be necessary to understand this effect.

4 Summary

Energy resolution in the NEXT-White TPC has been further studied, and a resolution near 1% FWHM is shown to be obtainable at 2615 keV, as predicted in the preceding study [12]. This

resolution was obtained over nearly the entire active volume, demonstrating the effectiveness of the continuous ^{83m}Kr-based calibration procedure implemented to correct for geometric and lifetime effects, and improved slightly with more restrictive fiducial cuts. A major obstacle remaining is the understanding of the observed "axial length effect" in which the measured energy of extended tracks decreases with increasing track length in the axial (drift) direction. While the effect can in principle be corrected for individual peaks, it must be better understood to ensure consistency across a wide range of energies.

Acknowledgments

References

[1] J. Schechter and J. W. F. Valle, *Neutrinoless Double beta Decay in SU(2)×U(1) Theories*, *Phys. Rev. D* **25** (1982) 2951.

[2] J. Gómez-Cadenas, J. Martín-Albo, J. Munoz Vidal, and C. Pena-Garay, *Discovery potential of xenon-based neutrinoless double beta decay experiments in light of small angular scale CMB observations*, *JCAP* **1303** (2013) 043, [arXiv:1301.2901].

[3] F. T. Avignone III, S. R. Elliott, and J. Engel, *Double beta decay, Majorana neutrinos, and neutrino mass*, *Rev. Mod. Phys.* **80** (2008) 481, [arXiv:0708.1033].

[4] J. J. Gómez Cadenas, J. Martín-Albo, M. Mezzetto, F. Monrabal, and M. Sorel, *The Search for Neutrinoless Double Beta Decay*, *Riv. Nuovo Cim* **35** (2012), no. 3 29–98.

[5] **NEXT** Collaboration, V. Álvarez et al., *The NEXT-100 experiment for neutrinoless double beta decay searches (Conceptual Design Report)*, arXiv:1106.3630.

[6] **NEXT** Collaboration, V. Álvarez et al., *NEXT-100 Technical Design Report (TDR): Executive Summary*, *JINST* **7** (2012) T06001, [arXiv:1202.0721].

[7] **NEXT** Collaboration, J. J. Gomez-Cadenas et al., *Present status and future perspectives of the NEXT experiment*, *Adv. High Energy Phys.* **2014** (2014) 907067, [arXiv:1307.3914].

[8] **NEXT** Collaboration, J. Martín-Albo et al., *Sensitivity of NEXT-100 to Neutrinoless Double Beta Decay*, *JHEP* **05** (2016) 159, [`arXiv:1511.09246`].

[9] **NEXT** Collaboration, V. Álvarez et al., *Near-Intrinsic Energy Resolution for 30 to 662 keV Gamma Rays in a High Pressure Xenon Electroluminescent TPC*, *Nucl. Instrum. Meth.* **A708** (2012) 101–114, [`arXiv:1211.4474`].

[10] **NEXT** Collaboration, V. Álvarez et al., *Initial results of NEXT-DEMO, a large-scale prototype of the NEXT-100 experiment*, *JINST* **8** (2013) P04002, [`arXiv:1211.4838`].

[11] **NEXT** Collaboration, F. Monrabal et al., *The Next White (NEW) Detector*, *arXiv: 1804.02409. Accepted by JINST* (2018) [`arXiv:1804.02409`].

[12] **NEXT** Collaboration, J. Renner et al., *Initial results on energy resolution of the NEXT-White detector*, *JINST* **13** (2018) P10020, [`arXiv:1808.01804`].

[13] **NEXT** Collaboration, G. Martínez-Lema et al., *Calibration of the NEXT-White detector using* ^{83m}Kr *decays*, *arXiv: 1804.01780. Accepted by JINST* (2018) [`arXiv:1804.01780`].